**Tailoring Electrode Microstructure via Ink Content to Enable Improved Rated Power Performance for Platinum Cobalt/High Surface Area Carbon Based Polymer Electrolyte Fuel Cells**

Tim Van Cleve,[a] Guanxiong Wang,[a] Mason Mooney,[a,c] C. Firat Cetinbas,[b] Nancy Kariuki,[b] Jaehyung Park,[b] Ahmed Farghaly,[b,d] Deborah Myers,[b] and K.C. Neyerlin[a*]

[a]National Renewable Energy Laboratory, Golden CO, 80401, USA

[b]Argonne National Laboratory, Lemont, IL 60439, USA

[c]The Ohio State University, Columbus OH, 43210 USA

[d]Assiut University, Assiut 71516, Egypt

*Corresponding Author

Address:

15257 Denver West Parkway

ESIF A340-08

Golden, CO 80401

Email: kenneth.neyerlin@nrel.gov

Tel: (720) 899-2439

Highlights (85 character limit)

- Ink water content (nPA:$H_2O$ ratio) primarily affects $O_2$ transport
- Ionomer coverage on catalyst has weaker effects for HSC-supported catalysts
- Higher ink water leads to smaller PtCo/HSC aggregate particles and lower $R_{nF}$
- 70wt% $H_2O$ PtCo/HSC MEA exceeds US DOE 2020 performance targets

Keywords

Polymer electrolyte fuel cells, ink solvent effects, $O_2$ transport, nano-CT, USAXS, ionomer-catalyst interface

**Abstract**

Improvements in polymer electrolyte fuel cell (PEFC) electrode performance have primarily focused on catalyst and ionomer developments, marginalizing the importance of catalyst ink formulation. Herein, the effect of ink formulation is examined across a series of cathodes comprised of PtCo supported on high surface area carbon (PtCo/HSC) and Nafion ionomer using an array of *in situ* electrochemical and *ex situ* characterization techniques. In contrast to prior work on Pt/Vu systems, ink water content had little effect on the electrochemically determined ionomer coverage for the PtCo/HSC electrocatalyst examined here. Characterization using nano-scale resolution X-ray computed tomography (nano-CT) demonstrated that water-rich ink formulations lead to a reduction in aggregate size (ionomer + PtCo/HSC), improving local $O_2$ transport. This understanding, combined with the use of a *commercially-available electrocatalyst* was used to produced state-of-the-art membrane electrode assemblies with Pt loadings of 0.03/0.08 $mg_{Pt}/cm^2$ on the anode and cathode respectively, having; i) > 1 $A/mg_{Pt}$ (0.9 $V_{iR\text{-}free}$, 150 kPa, 80°C, 100% RH, $H_2/O_2$), ii) 320 $mA/cm^2$ at 0.8 V, 150 kPa, 80 °C, 100% RH, $H_2$/Air), and iii) > 1 $W/cm^2{}_{elec}$ at rated power (0.67 V, 250 kPa, 94°C, 65% RH, $H_2$/Air) or < 0.11 $g_{Pt}/kW_{rated}$.

**Introduction**

Over the past several decades, significant advances in polymer electrolyte fuel cell (PEFC) performance and durability have enabled companies such as Toyota, Honda, and Hyundai to begin introducing hydrogen PEFC-powered vehicles into select markets. However, widespread commercialization is still impeded by the high cost of electrode components necessitating the development of cheaper and more efficient PEFCs. To spur further technological developments, the U.S. Department of Energy (DOE) has established ambitious performance targets for low-Pt loading PEFCs; i) mass activity >0.44 A/$mg_{Pt}$, ii) > 300 mA/$cm^2_{elec}$ at 0.8 V for $H_2$/air operation, iii) > 1.8 W/$cm^2_{elec}$ at rated power, all in an MEA with less than 0.125 mg/$cm^2$ total Pt loading [1].

To achieve these targets, three primary research pathways have emerged: (i) improved catalyst mass activity (A/$mg_{Pt}$) through electrocatalyst synthesis and/or post processing conditions [2–9], (ii) decreased oxygen transport resistance [10–13], occurring at or near the Pt reaction sites by improving Pt site location and accessibility, and (iii) incorporation of ionomers that improve conductivity (e.g. low EW ionomers) or modify the local electrocatalyst environment to enhance specific and mass activity [14–16]. While advancements have been plentiful, both in scientific understanding as well as PEFC performance, material improvements relating to any one of these focus areas tend to be discussed relative to their targeted focus, rather than in a broader context with membrane-electrode assembly (MEA) fabrication-related variables such as catalyst ink formulation and processing and subsequent electrode deposition, cell assembly, and electrode conditioning, all of which have been previously demonstrated to greatly impact performance [17,18,27–31,19–26].

Proper integration of materials to enable high performing PEFC operation has never been more crucial to realizing the individual improvements in electrocatalysts [32,33], supports [13,34–36], and ionomers [37,38]. Variables such as ink formulation (i.e., solvent identity and solvent ratios), processing method, ionomer chemistry, carbon morphology/porosity and even metal loading can impact the ink level

interactions of the materials set and subsequently alter the final electrode structure [20,21,23,39]. The resulting electrode structure can in turn influence active site accessibility and ORR activity as well as oxygen transport resistance and electrode proton conductivity. Optimization of ink formulation and electrode structure is often an iterative process in which conclusions from *in situ* performance/diagnostics and *ex situ* characterization (e.g., microscopy and tomography) establish structure-property relationships and inform future developments.

Previous reports have shown how changes in the ink solvent ratio impact ionomer-catalyst-solvent interactions leading to different rheological, morphological, and interfacial phenomena, which impact electrode microstructure and performance. For Pt/Vulcan carbon (Pt/Vu)-containing MEAs fabricated with a low equivalent weight (EW) perfluorosulfonic acid (PFSA) ionomer, Orfanidi *et al.* [40] observed that smaller ionomer aggregate structures and high alcohol content exhibited superior ORR and $O_2$-transport performance. Takahashi et al. [21] reported larger Pt/high surface area carbon (Pt/HSC) (TKK) catalyst aggregates present in higher water content inks correlated with increased heterogeneity of Nafion™ (D1020/D2020) ionomer in the electrode microstructure which led to improved bulk $O_2$ transport compared to alcohol-rich ink MEAs. Van Cleve et al. [26] demonstrated increasing ink water content leads to increased coverage on Pt/Vu, but local $O_2$ transport trends have a complex relationship due to competing effects of catalyst agglomerate break-up and stronger catalyst-ionomer interactions with higher ink water content MEAs. Additionally, a thorough study on the impact of ink content on the bulk-electrode transport resistance (i.e., through plane gas transport) of electrocatalyst layers containing platinum group metal (PGM)-free catalysts highlighted that changes in ionomer/electrocatalyst interactions and aggregation are strongly dependent on ink water content [41,42]. Generally, optimized ink formulations are specific to a particular set of materials (electrocatalyst, support, and ionomer), and it remains unclear how these process variables lead to enhanced performance across various electrode systems.

In this work, the effect of ink water content, *n*-propanol to water ratio (n-PA:water), on electrode microstructure and performance of MEAs containing state-of-the-art commercial catalyst (30 wt% PtCo/HSC, Umicore), D2020 (1000EW) ionomer, and Nafion™ 211 membrane (Ion Power) are examined. *In situ* and *ex situ* characterization of catalyst inks and MEAs describes how ink water content affects ionomer-catalyst interactions leading to morphological changes across multiple length scales. Specifically, CO displacement chronoamperometry and electrochemical impedance spectroscopy (EIS) experiments were utilized to directly measure ionomer coverage on various electrodes and describe the ionomer-catalyst interface at relevant conditions (80 °C, 150 kPa). These *in situ* electrochemical techniques have distinct advantages over more indirect, spatially-limited techniques like energy-dispersed X-ray spectroscopy (EDS) elemental maps generated by high resolution electron microscopy, which only provide detail about select regions of the electrode at one time. Additionally, X-ray scattering (USAXS and SAXS) and nano-scale resolution X-ray computed tomography (nano-CT) experiments provide complementary information about the electrode morphology at larger length scales describing PtCo catalyst particles, C particles, and aggregate size distributions (nm to 10s of µm). Ultimately, the superior performance of water-rich formulations can be attributed to the enhanced $O_2$ transport resulting from a more porous electrode microstructure with smaller aggregate particles.

**Experiment Methods**

**Fabrication of Catalyst Coated Membranes (CCMs)**

All catalyst inks were prepared using an established protocol [20,43]. Specifically, 30 wt% PtCo/HSC (Umicore) was dispersed in a mixture of deionized water (DI) and n-propanol (*n*-PA), resulting in a final concentration of 2.0 $mg_{Pt}$ $mL^{-1}$ solvent. Five different solvent ratios were investigated, such that the final PtCo/HSC cathode inks were prepared with 30, 50, 60, 70, and 80 wt% water in solvent. As a shorthand, samples will be defined by their ink solvent ratio using the notation nXwY, where X and Y correspond to the mass ratio of *n*-PA and $H_2O$, respectively. Dupont D2020 ionomer was then added to

the ink solution to give the desired ionomer to carbon (I/C) mass ratio of 0.9.[25] Catalyst inks were dispersed using 20 s of horn sonication followed by 20 min of bath sonication in ice water.[20] The cathode catalyst layer was ultrasonically sprayed onto Nafion™ NR211 membranes (Ion Power) heated to 80°C on a porous vacuum plate using a Sono-Tek spray station with 25kHz accumist nozzle, targeting catalyst loadings of either 0.04 $mg_{Pt}$ $cm^{-2}$ (for $O_2$ limiting current and 5$cm^2$ $H_2$/Air experiments), 0.10 $mg_{Pt}$ $cm^{-2}$ (for ECA and CO displacement experiments), and 0.30 $mg_{Pt}$ $cm^{-2}$ (for EIS measurements). Platinum loadings on individual electrodes were determined by XRF (Fisher XDV-SDD) are reported in supporting information. Anode electrodes were fabricated with Pt/HSC (TKK, TEC10E50E) dispersed in *n*-PA:water (62wt% water) with a 0.9 I/C and a 0.10 $mg_{Pt}$ $cm^{-2}$ loading.

**Membrane Electrode Assembly**

Once fabricated, MEAs with a cathode loading of 0.10 and 0.30 $mg_{Pt}$ $cm^{-2}$ were tested using a 50 $cm^2$ double/triple (anode/cathode) serpentine flow field to acquire mass and electrode area-specific oxygen reduction reaction (ORR) activities, electrochemically-active surface areas (ECA), and ionomer coverage via CO displacement and EIS experiments. High metals loadings are typical for ionomer loading measurements since both EIS and CO displacement experiments are very sensitive and higher ECA improves data reliability and reproducibility. Catalyst-coated membranes with cathode loadings of 0.04 $mg_{Pt}$ $cm^{-2}$ were utilized in 5 $cm^2$ differential cells to obtain oxygen limiting current and the resulting oxygen transport resistances [43–45]. The CCMs were sandwiched between either (i) two 50 $cm^2$ SGL29 BC gas diffusion layers (GDLs), at 25% compression, or (ii) two 5 $cm^2$ Freudenberg H23C8 GDLs at 18% compression relative to GDL thickness. The CCMs, GDLs, and polytetrafluoroethylene (PTFE) gaskets were then placed between the flow fields and the bolts tightened to 40 inch-pounds. SGL 29 BC GDLs were used in characterization experiments following established protocols [26].

***In situ* Electrochemical Diagnostics**

**MEA Break-In and Conditioning.** Previous work demonstrated how break-in and voltage recovery protocols can improve the overall cell performance [43]. In this study, PtCo/HSC MEAs were fully conditioned following a break-in and five 2-hr voltage recovery cycles at 40°C, 150% RH, and 0.1V.

**$H_2/O_2$ Polarization Curves in 5cm$^2$ Differential Cell**. The test protocol involved measuring the current-voltage (I-V) curves from 0.4 V to open circuit voltage (OCV) at 80 °C and 100 kPa $O_2$ partial pressure (150 kPa total pressure) and 100% relative humidity (RH) for 4 min per point (average of last 1 min used) in the anodic direction. Pure $H_2$ and $O_2$ gases were flowed at 700 sccm through anode and cathode gas feeds, respectively (stoichiometries >15 and >7). The ORR mass activities were reported at 0.90 V after applying high-frequency resistance (HFR) and hydrogen cross-over corrections [43].

**$H_2$/Air Polarization Curves in 5cm$^2$ Differential Cell**. The test protocol involved measuring the I-V curves from 0.3 V to OCV at 80 °C and at 150 kPa total pressure with 75% RH for 4 min per point (average of last 1 min used) in the anodic direction with gases fed at constant rate of 700 sccm. Currents were normalized by metal loading determined by X-ray fluorescence spectrometry (XRF).

**$O_2$ Limiting Current Experiments**. Limiting current measurements were performed on 5cm$^2$ differential cell MEAs at 80 °C and 75% RH, with oxygen mole fractions of 0.02, 0.03 and 0.05. The limiting current was obtained at total cell pressures of 100, 150, 200 and 300 kPa. Limiting current was measured at constant voltages, held for 3 min, of 0.30, 0.24, 0.18, 0.12, and 0.06 V. Due to the impact of hydrogen evolution on current densities obtained below 0.1 V, the maximum of the resulting current densities above 0.12 V was reported as the limiting current. Additional details on the procedure were previously described by Baker et. al [45].

**CO Displacement Chronoamperometry.** The test protocol involved measuring the transient current response (I-t) resulting from the introduction of CO to an equilibrated electrode held at a constant potential.[24] During this process, adsorbed cationic/anionic species are displaced through oxidative/reductive process and the resulting displacement charge ($q_{dis}$) corresponds to the amount of

charged surface species present at a specific potential. Experiments were conducted at 80°C while the electrode was held at 0.1V, 0.2V, 0.3V, 0.4V, and 0.5$V_{cell}$. Sulfonate coverages were determined by normalizing the displacement charges measured at 0.4 $V_{cell}$ by CO stripping charge ($Q_{CO}$).

**CO Stripping Voltammetry**. Pt ECA was determined by integrating the CO stripping charge ($Q_{CO}$) obtained from cyclic voltammetry (CV) immediately following CO displacement experiments. The cathode feed was purged with pure $N_2$ at 0.25 $L_{std}$ $min^{-1}$ prior to the first anodic sweep. CVs were performed at 80 °C under $H_2/N_2$ sweeping from 0.05 to 0.9 V at 20 mV $s^{-1}$. An area-specific charge of 420 μC $cm^{-2}$ was assumed for converting the CO stripping charge to ECA.

**AC Impedance Experiments**. Electrochemical impedance spectroscopy (EIS) experiments were prepared on fully conditioned 50 $cm^2$ MEAs with 0.3$mg_{Pt}$ $cm^{-2}$ using a Gamry Reference 3000 Potentiostat connected to a Gamry 30k Booster. EIS experiments were conducted at 80 °C with 1 atm pure $H_2$ and $N_2$ flowing at 100 cc $min^{-1}$ at anode and cathode gas lines, respectively. Experiments were run at 10%, 25%, 50%, 75%, and 100% RH with 30-60 min equilibration time before each measurement. EIS were measured 50kHz-50mHz at 0.45V and 0.2V vs RHE with ±10mV oscillations for CO-free and CO-doped experiments, respectively. Cathodes were exposed to 1% $CO/N_2$ feed for 15 minutes to allow for CO adsorption, then purged with pure $N_2$ prior to CO-doped experiments. Residual CO was oxidized after CO-doped EIS experiments and before CO-free EIS measurements.

**High Temperature Polarization Measurements.** 50$cm^2$ MEAs were prepared 60, 70, and 80 wt% $H_2O$ PtCo/HSC ink formulations having nominal loadings of 0.08mgPt/$cm^2$ at the cathode. Anodes with 0.03$mg_{Pt}/cm^2$ loadings were prepared from Pt/HSC (as described earlier). Catalyst layers were ultrasonically sprayed onto a 10 μm PFSA membrane, which was then sandwiched between two Freudenberg H23C8 GDLs. MEAs were subjected to the same conditioning protocols described earlier and $H_2$/Air performance was measured at 80 and 94°C in a counter flow configuration with gas stoichiometries of 1.5 and 2.0 at the anode and cathode, respectively [11,46].

**MEA Characterization**

**Ultra-Small Angle and Small Angle X-Ray Scattering (USAXS and SAXS) Experiments.**

The X-ray scattering data were collected on a combined Bonse-Hart (USAXS) and pinhole (SAXS) instrument at beamline 9-ID-C at the Advanced Photon Source (APS) located at Argonne National Laboratory. Details regarding the optics and instrumentation have been previously reported [47]. The X-ray beam was monochromatized via a pair of Si(220) crystals to an energy of 21 keV. The beam spot size for USAXS was 0.8 × 0.6 mm (horizontal x vertical) and 0.8 × 0.2 mm for SAXS. The X-ray beam exposure times for each sample were 90 s for USAXS, and 30 s for SAXS. The samples were prepared by removing a section of the cathode catalyst layer from the membrane with single-sided, transparent Scotch™ tape using a press-peel technique. The samples were then supported in a custom-made sample holder for the USAXS/SAXS measurements. Patterns collected on a blank piece of tape were subtracted from the patterns acquired for the samples during data reduction. The data were corrected and reduced with the NIKA software package,[48] and data analysis was conducted using the IRENA software package [49]. Both packages were run on IGOR Pro 7.0 (Wavemetrics). Particle size distributions were obtained from the measured scattering data using the maximum entropy (MaxEnt) method,[50] which involves a constrained optimization of parameters to solve the scattering equation:

$$I(q) = |\Delta\varrho|2 \int |\mathrm{F(q,r)}|2 \left(\mathrm{V\ (r)}\right)2\ \mathrm{Np\ (r)dr}_{int} \qquad [1]$$

Where, I(q) is the scattered intensity, ϱ is the scattering length density of the particle, F(q, r) is the scattering function at scattering vector q of a particle of characteristic dimension r. V is the volume of the particle, and Np is the number density of particles in the scattering volume.

**Nano-CT Experiments.**

X-ray radiographs of PtCo/HSC electrode (extracted from the cathode of an MEA, refer to Ref. [51,52] for more details) were acquired using the Xradia nano XCTS100 TXM at beam line 32-ID-C of the APS. Employing a fly-scan technique, 1080 projection images were acquired over 180° rotation. The projection

images were reconstructed into a 3D image sequence with ~20-nm voxel size using Tomopy and Astra.[53,54] Following the procedure in Refs. [55–58] the $Cs^+$-exchanged sample was scanned in both absorption and Zernike phase contrast modes. The phase contrast mode resolves the overall morphology of the solid (a mixture of C, Pt, ionomer and primary pores below the resolution of nano-CT) while the absorption contrast images provide an intensity map of the high electron-density materials within the sample (i.e., $Cs^+$ signal indicates the ion-exchanged ionomer). It should be noted that the intensity map in absorption contrast images also includes the contribution from the catalyst particles (especially the large catalyst particles observed as small bright dots), but due to the small volume of the catalyst in comparison to ionomer, the signal from the catalyst particles are ignored.

**Results/Discussion**

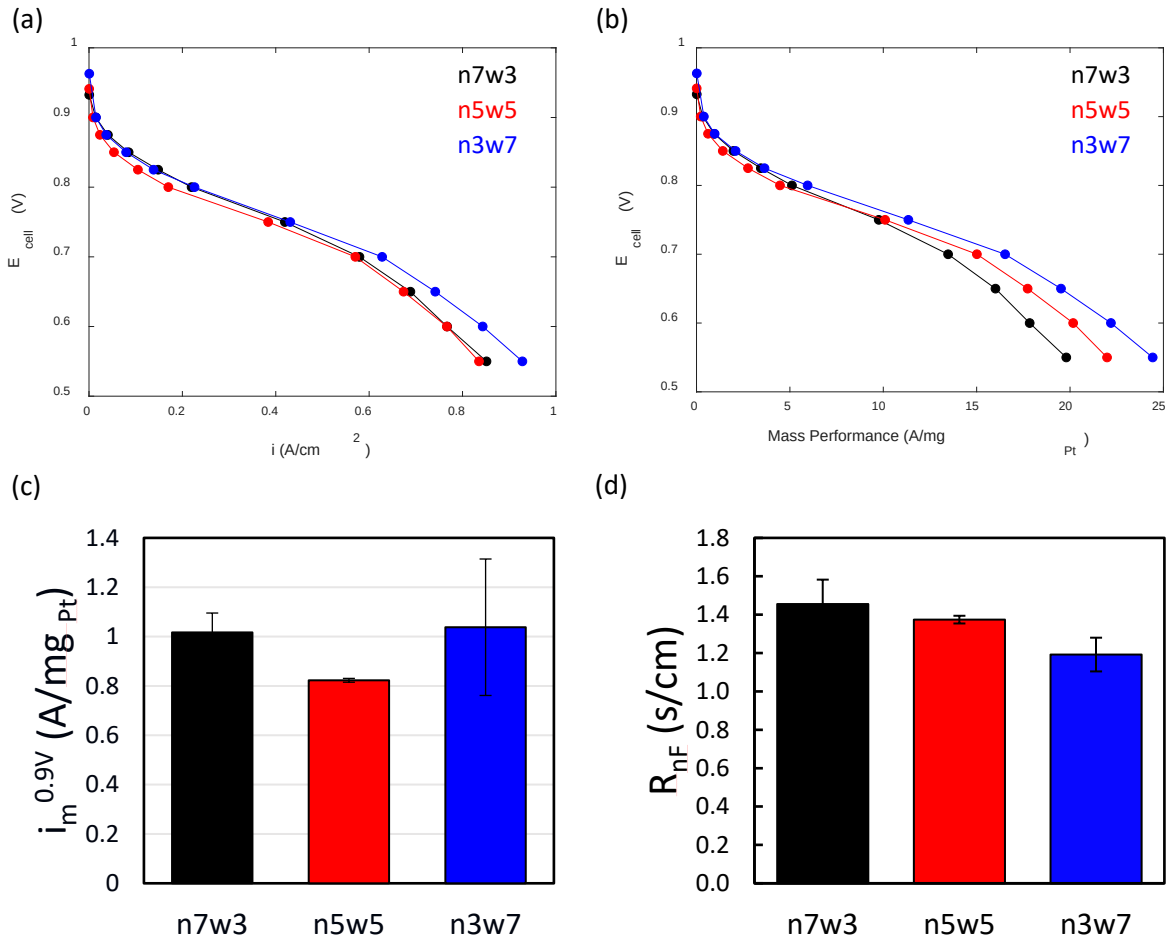

**Figure 1**. a) Nominal and b) Pt mass-based $H_2$/Air performance of various PtCo/HSC MEAs measured at 150 kPa, 80 °C, and 75% RH in 5cm$^2$ differential cell experiments (L≈0.04mg$_{Pt}$/cm$^2$, GDL: H23C8). c) Mass activity measured at 0.9V$_{iR\text{-}free}$ as a function of solvent ratio. High stoichiometric flows were used (700 sccm at both anode and cathode). (d) Non-Fickian $O_2$ transport resistance ($R_{nF}$) measured at 75% RH as a function of solvent ratio. Error bars represent standard deviation from at least two independent measurements.

Figures 1a and 1b compare the nominal and Pt mass-based performance of n7w3, n5w5, and n3w7 PtCo/HSC MEAs during $H_2$/air polarization experiments performed at 150 kPa, 80 °C, and 75% RH. All samples exhibit similar performance at high cell voltages (V>0.8V), which is supported by comparable mass activities ($i_m^{0.9V}$) around 1 A/mg$_{Pt}$ (Figure 1c) and similar Tafel slopes (Figure S1) observed in $H_2/O_2$ experiments. However, MEAs with electrodes made from water-rich inks (70 wt% $H_2O$) exhibit higher current densities especially at cell voltages below 0.6 V where $O_2$ transport dominates. Limiting current experiments corroborate these performance trends with the lowest non-Fickian (pressure-independent) $O_2$ transport resistance ($R_{nF}$) observed for the 70 wt% $H_2O$ MEAs, as shown in Figure 1d. Literature has previously identified at least three contributing factors to $R_{nF}$; i) the ionomer-catalyst interface [13,59–61], ii) the total number of accessible active sites [62,63], iii) transport resistance inside the agglomerates as capillary condensed water starts filling the pores inside the agglomerates [56,64]. Since all PtCo/HSC MEAs have nearly equivalent ECAs (see SI Figure S2), and the majority of particles are located in the pores of the high surface area carbon, reducing, but not necessarily eliminating contributions from the catalyst ionomer interface, differences in $R_{nF}$ are most likely stemming from increased diffusion resistance through the aggregate/agglomerate microstructure.

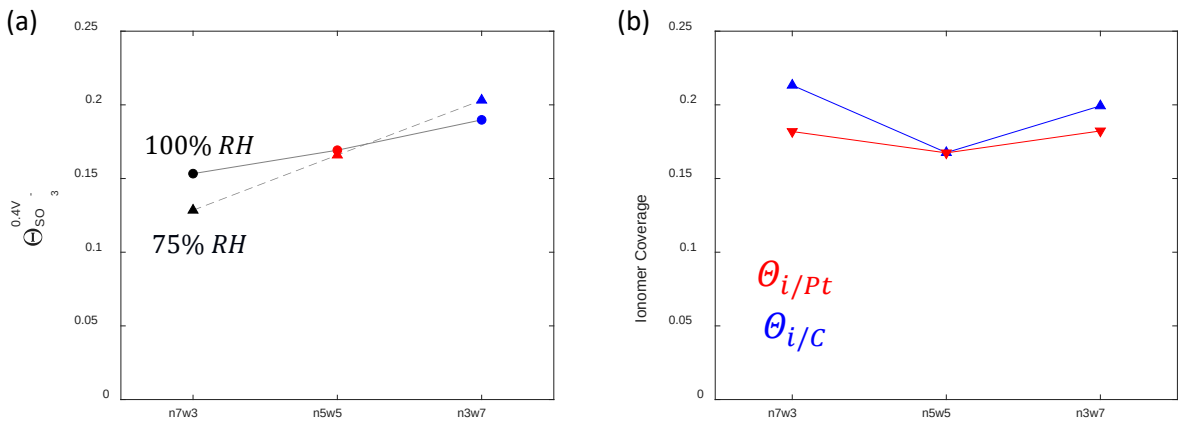


**Figure 2.** a) Sulfonate coverage on PtCo/HSC electrodes measured by CO displacement at 0.4$V_{cell}$ at 75% (dashed) and 100% RH (solid). b) Ionomer coverage on Pt and C measured as a function of ink formulation with electrochemical impedance spectroscopy.

Despite this hypothesis, *in situ* electrochemical techniques, CO displacement chronoamperometry and EIS were used to probe sulfonate adsorption (on Pt) and ionomer coverage (on Pt and C) under realistic operating conditions (80 °C and 150 kPa) to glean potential changes in the Pt/ionomer interface.[24,26,65,66] Sulfonate ($-SO_3^-$) coverages were calculated by normalizing the CO displacement charge measured at 0.4$V_{cell}$ to the ECA (determined by CO stripping voltammetry obtained at the same T, P, and RH). Figure 2a compares the sulfonate coverage on fully conditioned PtCo/HSC MEAs at several RHs. At 100% RH, sulfonate coverage slightly increases with water content of catalyst ink ranging from 0.15 to 0.19 for n3w7 and n3w7 MEAs, respectively. Similarly, sulfonate coverage was also shown to slightly increase with ink water content for experiments performed at 75% RH ($0.13 < \Theta < 0.21$). These sulfonate coverages measured at high relative humidity are slightly higher than the previously-reported sulfonate coverages of ca. 0.10 on 30 wt% Pt/HSC (TKK) MEAs measured at 40 °C, 80% RH.[24] In that study, the ink composition was not specified, but these differences could potentially be explained by different electrode fabrication, C support morphology, and/or the experimental conditions at which the data was acquired. Regardless of this trend, for materials where electrocatalysts are located inside carbon pores, it appears difficult to correlate ionomer coverage/interaction with performance metrics such as local transport resistance. This is a stark contrast to electrodes fabricated with externally accessible

carbon supported electrocatalysts, such as Pt/Vu, which clearly show increased Pt sulfonate adsorption with increasing ink water content [26].

In addition to Pt sulfonate coverage, ionomer coverages on Pt and C were calculated from changes in double-layer capacitance measured by EIS [26,65]. Using CO to block capacitive contributions from Pt and RH to control contributions from $H_2O$ adsorption, it is possible to determine how much the Pt-ionomer and C-ionomer interfaces contribute to the overall double-layer capacitance. Figure 2b compares ionomer coverages on Pt and C as a function of ink water content. Ionomer coverage on C is only slightly higher than coverage on Pt (25% and 20%, respectively) across all samples and comparatively much lower than ionomer coverages measured on Pt/Vu MEAs (60-90% on C and 30-50% on Pt) [26,65]. Lower coverages for HSC supported electrocatalysts are related to limited ionomer intrusion into the C pore structure, having been described earlier [21,65]. Further examination of Figure 2b reveals ionomer coverage to be a weak function of ink solvent ratio. These AC impedance results suggest ionomer coverages on Pt and C do not appreciably change with ink content for these PtCo/HSC electrodes, however CO displacement results suggest there may be some conformational changes of the local ionomer structure near Pt sites consistent with increased exposure of chains for higher ink water content formulations. These orientational effects have previously been demonstrated for unbound ionomer dispersions [67–70]. Having systematically ruled out the possibility for interfacial phenomena to contribute to changes in $R_{nF}$ for electrodes with internally-distributed Pt catalyst sites focus shifts to aggregation and microstructural effects.

To investigate the effect of ink solvent ratio on catalyst-ionomer microstructure, X-ray scattering measurements were performed on catalyst inks and MEAs to monitor changes in catalyst particle, C aggregate, and agglomerate sizes as a function of ink formulation. X-ray scattering experiments performed on catalyst inks and electrode layers yield similar results (Figure S4); for this reason, the discussion will focus on the X-ray scattering results for the assembled electrodes. Particle size distributions (PSDs) for

catalyst and C particles can be determined by fitting the X-ray scattering regions between Q < 0.026 $Å^{-1}$ (1.5 – 10 nm) and 0.02 $Å^{-1}$ < Q < 0.001 $Å^{-1}$ (10 – 250 nm), respectively, corrected using an exponential (agglomerate scattering) background. All ink formulations gave similar PtCo PSDs with an average size of 4.1-4.2 nm regardless of the ink formulation (Figure 3b). Similarly, the PSDs of small C particles (20 – 100 nm), the reported size range of the primary C particles,[71–73] do not appear to significantly change with ink solvent ratio (Figure 3c), as expected. At slightly larger length scales (100-300 nm), in the size range reported for clusters and chains of fused primary carbon particles[71–73] (termed aggregates here[74]), MEAs made using water-rich inks show better long-range order and smaller cluster sizes. Furthermore, differences in the USAXS spectra become more discernable at larger length scales (d > 1000 nm), or in the low-q scattering intensity region describing agglomerate structure (Figure 3b). The higher scattering intensity observed for *n*-PA rich formulations indicates the presence of larger agglomerate structures in the electrode. This observation corroborates earlier results that show stronger interactions between ionomer and catalyst particles, which stabilize smaller aggregate particles in $H_2O$-rich catalyst inks [39].

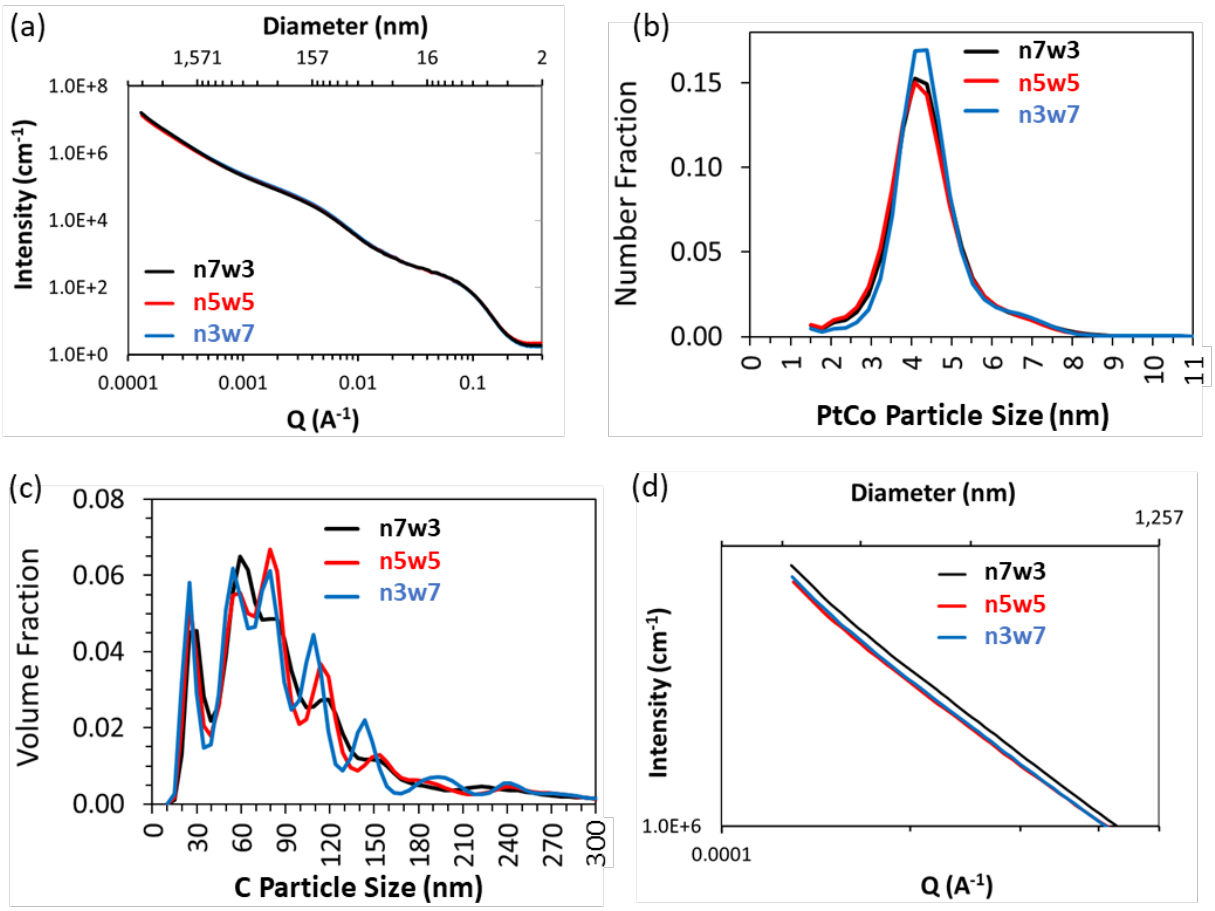


**Figure 3.** a) X-ray scattering profile for various PtCo/HSC electrodes (30-70 wt% ink $H_2O$ content). b) Particle size distributions of PtCo catalyst particles and c) C particles determined from fitting of the X-ray scattering profiles. d) USAXS profiles in the large agglomerate region (d > 1µm) for various PtCo/HSC electrodes.

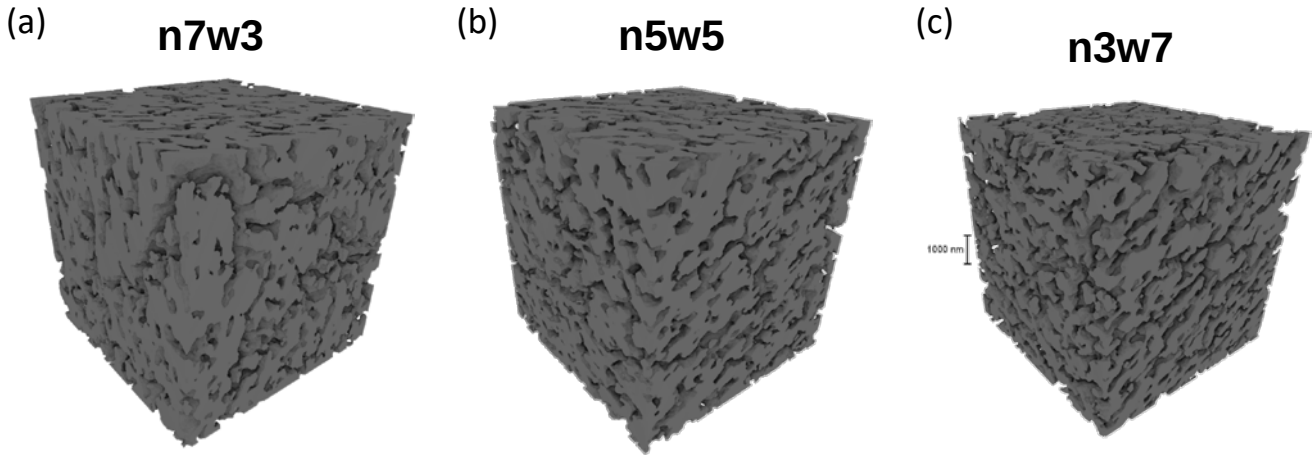


**Figure 4.** Segmented nano-CT phase contrast mode data for $Cs^+$ ion-exchanged PtCo/HSC electrodes prepared using 30wt%, 50wt%, and 70wt% $H_2O$ catalyst-ionomer ink formulations.

To better resolve the differences in electrode structure, nano-CT characterization was performed on the electrodes prepared using n7w3, n5w5, and n3w7 catalyst-ionomer inks. Data collected in phase contrast mode facilitates imaging of the secondary pore morphology and the structure of the solid electrode comprising C, Pt, and ionomer, as show in Figures 4a-c. Comparing the nano-CT data for electrodes prepared from *n*-PA rich (30wt% $H_2O$) and $H_2O$ rich inks (70wt% $H_2O$), there is a clear qualitative trend showing increased ink water content leads to a more porous electrode structure with smaller agglomerates, consistent with the observations from the USAXS experiments. Quantitative analysis of these microstructures show electrodes made from water-rich inks exhibit an abundance of smaller C aggregates Figure S5a) and higher effective diffusion coefficients in all directions (Figure S5b), which explains the observed improved gas transport compared to *n*-PA rich electrodes.

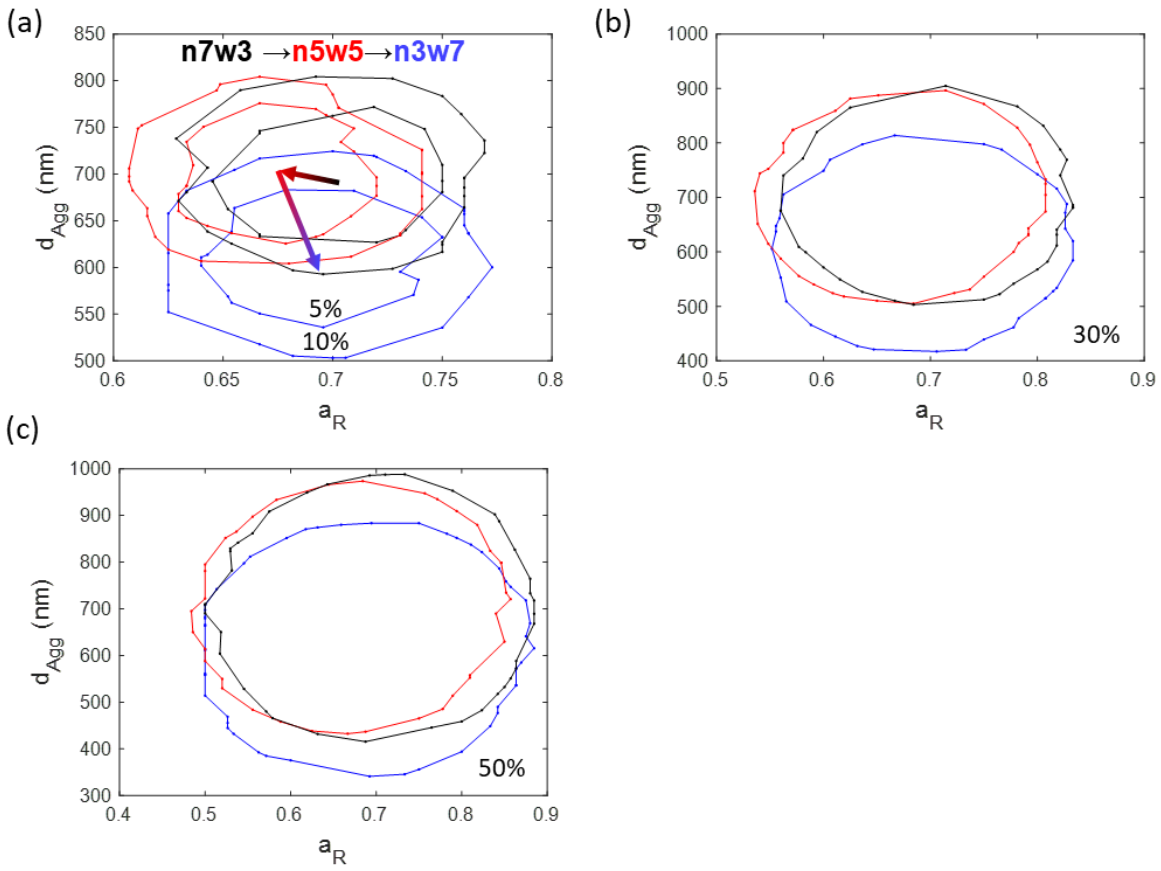


**Figure 5.** Enclosed regions show the distribution of aggregate diameters ($d_{Agg}$) and aspect ratios of the middle 5 and 10% (a), 30% (b), and 50% (c) of PtCo/HSC aggregates extracted from segmented nano-CT

data on electrodes prepared from 30 (black), 50 (red), and 70 wt% (blue) $H_2O$ inks using watershed separation technique.

Recent work by Cetinbas *et al.* [52] demonstrated that local $O_2$ transport can also depend on aggregate size and shape, which were found to vary with ink formulation and electrode fabrication method. Utilizing a similar approach, detailed information about the aggregates in PtCo/HSC electrodes was extracted from nano-CT data using a watershed separation technique (described previously).[52] The average particle diameter ($d_{agg}$) and aspect ratio ($a_R$ = 1 for sphere) were determined for at least 1200 aggregates identified in each electrode volume. Distributions of PtCo/HSC aggregates (shown in Figure S6) indicate a non-normal distribution with aggregate diameters ranging from 100 to 1450 nm and aspect ratios from 0.2 to 1. To assess ink content effects on the size and shape of aggregate particles and better describe the population, a sorting algorithm was employed to identify the middle *p%* of particles (see details in SI). Figure 5a demonstrates how median aggregate peaks change with ink formulation; specifically, the concentric circles correspond to regions that enclose the middle 5 and 10% of aggregates for each electrode. Electrodes prepared using alcohol-rich ink (n3w7) exhibit the largest and most spherical aggregates. While increasing ink water content to 50 wt% has a negligible impact on aggregate diameter, a slight shift to more oblong/deformed shapes is observed. At 70 wt% ink water content, a significant drop in the average aggregate diameter is observed. These trends hold when comparing larger proportions of aggregates (e.g., 30 and 50%) as shown in Figures 5b and 5c. The shift to less spherical particles and smaller aggregate sizes have previously been shown to reduce local $O_2$ transport for electrocatalysts located within the carbon support [52]. This is consistent with our experimental observations. As shown in Figure 1d, $R_{nF}$ decreases as water content is increased from 30 to 50 wt%, due to the more oblong aggregate shapes (Figure 5a-c) and then as water content is further increased from 50 to 70 wt%, $R_{nF}$ is again reduced, this time due to a reduction in aggregate size.

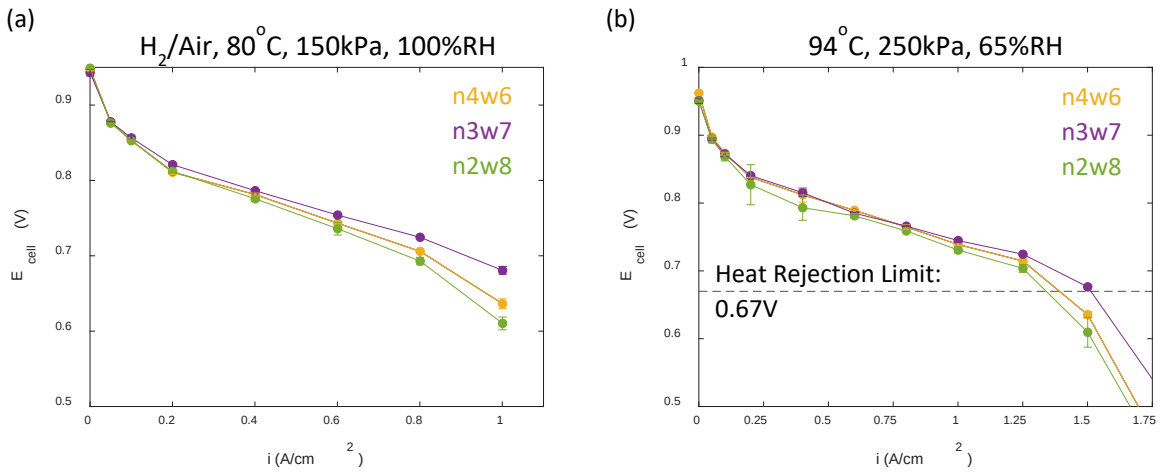


**Figure 6.** a) $H_2$/Air polarization curves measured for high-performance PtCo/HSC MEAs (H23C8 GDLs) with various ink water content (60 wt%, 70 wt%, and 80 wt% $H_2O$) and cathode loading of 0.08 $mg_{Pt}/cm^2$ at standard saturated conditions (80 °C, 150 kPa). b) $H_2$/Air performance of 50 $cm^2$ PtCo/HSC MEAs measured under heat rejection conditions (94 °C, 65% RH, and 250 kPa). Gases were fed at stoichiometric ratios of 1.5 and 2.0 at anode and cathode, respectively. Error bars correspond with the standard deviation of 3 experiments performed on different MEAs.

Having demonstrated the superior performance of water-rich ink formulations for this particular material set (30 wt% PtCo/HSC catalysts with D2020 ionomer and I:C of 0.9), several CCMs with 0.08 $mg_{Pt}/cm^2$ cathode loading (and 0.03 $mg_{Pt}/cm^2$ anode loading) were prepared for testing using a modified MEA design in counter-flow configuration (see *Experimental* section). To fine tune the best ink formulation, 60, 70, and 80 wt% $H_2O$ inks were used. Figure 6a compares the $H_2$/Air performance at 80 °C and 100% RH for these 50 $cm^2$ MEAs. Despite the differences in materials (membrane, loading, and hardware), MEAs prepared using 70 wt% $H_2O$ inks again exhibited superior performance at high current densities. The reduced performance for the 80 wt% $H_2O$ MEA could be due to a continued increase in ionomer phase segregation, the onset of which is shown for 70 wt% in Figures S6a-c [26,40]. The higher cathode loadings of 50$cm^2$ MEAs compared to 5$cm^2$ MEAs (shown in Figure 1) reduce the $O_2$ transport losses experienced at high current densities (~1A/$cm^2$), an effect described in detail elsewhere [13].

Figure 6b shows results from $H_2$/Air polarization curves performed at 94 °C, 65% RH, and 250 kPa. Here, the 70 wt% $H_2O$ MEA achieved a current density of 1.5 A/$cm^2$ at 0.67 $V_{cell}$ exceeding the power

density of 1 W/cm$^2$ with a low total Pt loading (compared to DOE targets in Table S3). Table 1 summarizes the PEFC performance of n4w6, n3w7, and n2w8 PtCo/HSC MEAs compared to other state-of-the-art MEAs. In general, these electrodes exhibited slightly higher kinetic performance (since measurements were performed in the anodic direction) and comparable $H_2$/air activity at saturated 80°C and heat-rejection conditions.

While our particular catalyst ink formulation (catalyst, ionomer, solvent combination) may not exhibit the best PEFC performance ever reported, this study illustrates that significant improvements in power density and efficiency can be achieved by understanding the effect of process variables such as ink solvent ratio on electrode structure and performance. Such insights will help facilitate rapid incorporation of promising materials (catalysts, ionomers, membranes, diffusion media, etc.) into high performance PEFC architectures.

**Table 1: Comparison of PEFC Performance with State-of-the-Art MEAs**

| Catalyst | Ink Content | Pt Content | Cathode Loading | Total Pt Loading | Mass Activity | Activity at 0.8V (80°C, 100% RH 150kPA$_{abs}$) | Power Density (0.67 V, 94°C, 65% RH 250kPa$_{abs}$) | Reference |
|---|---|---|---|---|---|---|---|---|
| | nPa:$H_2O$ | g/kW (rated) | mg/cm$^2$ | mg/cm$^2$ | A/mg$_{Pt}$ @ 0.9V | A/cm$^2$ | W/cm$^2$ | |
| PtCo/HSC | 4:6 | 0.118 | 0.077 | 0.107 | 1.26$^{*,@}$ | 0.274 | 0.932 | This Work |
| PtCo/HSC | 3:7 | 0.107 | 0.078 | 0.108 | 1.27$^{*}$ | 0.321 | 1.013 | This Work |
| PtCo/HSC | 2:8 | 0.122 | 0.077 | 0.107 | 1.19$^{*}$ | 0.267 | 0.900 | This Work |
| $L1_0$-PtCo/Vu | | 0.171 | 0.10 | 0.2 | 0.67$^{\%}$ | 0.32$^{\%}$ | 1.17$^{\%,\wedge}$ | [75] |
| PtCo/HSC | | 0.234 | 0.08 | 0.230 | 0.6$^{\&}$ | 0.245$^{\&}$ | 0.981$^{\&}$ | [14] |
| PtCo/Vu | | 0.124 | 0.10 | 0.125 | 0.62 | 0.2 | 1.005 | [76] |
| PtCo/KB | | 0.124 | 0.1 | 0.125 | 0.7 | 0.385 | 1.005 | [11] |
| PtCo/HSC-f | | 0.063 | 0.06 | 0.125 | 0.7 | 0.4 | 1.34 | [11] |
| PtCo/HSC-a | | 0.098 | 0.1 | 0.125 | 0.65 | 0.3 | 1.275 | [77] |

$^{*}$Measured during anodic sweep
$^{@}$Mass activity measured during cathodic sweep around 0.9 A/mg$_{Pt}$ [43]
$^{\&}$Stoichiometric flows of 2/2 instead of 1.5/2 typical for other measurements and 10cm$^2$ cell area
$^{\%}$Obtained from differential cell measurements (5cm$^2$)
^Obtained from differential cell measurements 0.67 V, 75% RH, 250 kPa, 80$^o$C.

**Conclusion**

*Ex situ* characterization of catalyst inks (comprising Nafion™ D2020 ionomer, 30 wt% PtCo/HSC, and n-PA/$H_2O$) and electrode layers along with *in situ* electrochemical testing of MEAs demonstrated that ink water (and alcohol) content has a significant impact on electrode microstructure and cell performance. X-ray scattering and X-ray nano-CT results revealed that water-rich inks lead to smaller average aggregate/agglomerate size and a more porous electrode structure, which improves $O_2$ transport within the aggregate and through the catalyst layer, respectively. While *in situ* electrochemical techniques identified stronger sulfonate adsorption on Pt with increasing water content along with moderate differences in ionomer coverage on Pt and C, neither effect alters local oxygen transport for electrocatalysts where Pt is located within the pores of the support.

Using a commercially available electrocatalyst and ionomer, modifying only the ink formulation, 50 $cm^2$ MEAs prepared with a 70 wt% $H_2O$ ink exhibited similar performance compared to state-of-the-art electrodes containing novel catalysts [75,76], ionomers[14], and C supports[11,77]. This work illustrates the importance of catalyst ink formulation in determining overall fuel cell performance. The insights from this study provide useful guidelines to facilitate the rapid incorporation and optimization of novel high-performance materials for future PEFC advances. Such considerations are also critical for the development of heavy-duty PEFC applications where fuel efficiency and durability are key performance metrics.

**Supporting Information**

The Supporting Information is available free of charge on the Publications website at DOI:

Metal loadings determined by XRF, Tafel plots, ECA measured by CO stripping voltammetry, sulfonate and ionomer coverages, average catalyst particle and aggregate sizes from X-ray scattering, X-ray scattering profiles of catalyst inks and electrode layers, pore volume distribution and effective diffusion coefficients calculated from the reconstructions of phase-contrast nano-CT images, absorption-contrast images and ionomer distributions from nano-CT, mass activities for different MEA loadings, MEA performance comparisons to DOE targets

**Acknowledgements**

This work was authored in part by Alliance for Sustainable Energy, LLC, the manager and operator of the National Renewable Energy Laboratory for the U.S. Department of Energy (DOE) under Contract No. DE-AC36-08GO28308. This work was also supported in part by the U.S. Department of Energy, Office of Science, Office of Workforce Development for Teachers and Scientists (WDTS) under the Science Undergraduate Laboratory Internship (SULI) program. The submitted manuscript was also created, in part, by U Chicago Argonne, LLC, operator of Argonne National Laboratory, a DOE Office of Science laboratory, under Contract DEAC02-06CH11357. Funding was provided by DOE Office of Energy Efficiency and Renewable Energy, Fuel Cell Technology Office, under the Fuel Cell Performance and Durability (FC-PAD) Consortium, technology manager Greg Kleen. The X-ray tomography experiments were performed at beamline 32-ID-C and the X-ray scattering experiments at beamline 9-ID-C at the Advanced Photon Source at Argonne National Laboratory. Use of the Advanced Photon Source, an Office of Science user facility operated by Argonne National Laboratory, is supported by the U.S. Department of Energy, Office of Science, Office of Basic Energy Sciences, under Contract No. DE-AS02-06CH11357. The authors would like to thank Jan Ilavsky, Ivan Kuzmenko, and Vincent De Andrade of the Advanced Photon Source. The authors appreciate the frequent insightful discussions with Dr. Scott Mauger and Mike Ulsh at NREL as well as Dr. Ahmet Kusoglu, Dr. Adam Weber, and Anamika Chowdhurry at LBNL. While we do not endorse any materials presented in this study, we wish to thank Umicore for the use of their electrocatalysts. The views expressed in the article do not necessarily represent the views of the DOE or the U.S. Government.

## References

[1] DOE, Hydrogen Storage Technologies Roadmap Fuel Cell Technical Team Roadmap, (2017). www.uscar.org. (accessed May 31, 2020).

[2] L. Guetaz, M. Lopez-Haro, S. Escribano, A. Morin, G. Gebel, D.A. Cullen, K.L. More, R.L. Borup,

Catalyst-Layer Ionomer Imaging of Fuel Cells, ECS Trans. 69 (2015) 455–464. https://doi.org/10.1149/06917.0455ecst.

[3] R.K. Ahluwalia, X. Wang, A.J. Steinbach, Performance of advanced automotive fuel cell systems with heat rejection constraint, J. Power Sources. 309 (2016) 178–191. https://doi.org/10.1016/j.jpowsour.2016.01.060.

[4] N. Becknell, Y. Son, D. Kim, D. Li, Y. Yu, Z. Niu, T. Lei, B.T. Sneed, K.L. More, N.M. Markovic, V.R. Stamenkovic, P. Yang, Control of Architecture in Rhombic Dodecahedral Pt-Ni Nanoframe Electrocatalysts, J. Am. Chem. Soc. 139 (2017) 11678–11681. https://doi.org/10.1021/jacs.7b05584.

[5] Y. Kang, J. Snyder, M. Chi, D. Li, K.L. More, N.M. Markovic, V.R. Stamenkovic, Multimetallic core/interlayer/shell nanostructures as advanced electrocatalysts, Nano Lett. 14 (2014) 6361–6367. https://doi.org/10.1021/nl5028205.

[6] J. Li, Z. Xi, Y.T. Pan, J.S. Spendelow, P.N. Duchesne, D. Su, Q. Li, C. Yu, Z. Yin, B. Shen, Y.S. Kim, P. Zhang, S. Sun, Fe Stabilization by Intermetallic L10-FePt and Pt Catalysis Enhancement in L10-FePt/Pt Nanoparticles for Efficient Oxygen Reduction Reaction in Fuel Cells, J. Am. Chem. Soc. 140 (2018) 2926–2932. https://doi.org/10.1021/jacs.7b12829.

[7] and V.R.S. Chen, C., Y. Kang, Z. Huo, Z. Zhu, W. Huang, H. L. Xin, J. D. Snyder, D. Li, J. A. Herron, M. Mavrikakis, M. Chi, K. L. More, Y. Li, N. M. Markovic, G. A. Somorjai, P. Yang, directions. At low T , in the present classical theory without randomness, S, Science (80-. ). 343 (2014) 1339–1343. https://doi.org/10.1126/science.1249061.

[8] S.M. Alia, S. Pylypenko, A. Dameron, K.C. Neyerlin, S.S. Kocha, B.S. Pivovar, Oxidation of Platinum Nickel Nanowires to Improve Durability of Oxygen-Reducing Electrocatalysts, The Electrochemical Society, 2019. https://doi.org/10.1149/2.0081605jes.

[9] S.M. Alia, C. Ngo, S. Shulda, M.-A. Ha, A.A. Dameron, J.N. Weker, K.C. Neyerlin, S.S. Kocha, S. Pylypenko, B.S. Pivovar, Exceptional Oxygen Reduction Reaction Activity and Durability of Platinum–Nickel Nanowires through Synthesis and Post-Treatment Optimization, ACS Omega. 2 (2017) 1408–1418. https://doi.org/10.1021/acsomega.7b00054.

[10] N. Nonoyama, S. Okazaki, A.Z. Weber, Y. Ikogi, T. Yoshida, Analysis of Oxygen-Transport Diffusion Resistance in Proton-Exchange-Membrane Fuel Cells, J. Electrochem. Soc. 158 (2011) B416. https://doi.org/10.1149/1.3546038.

[11] V. Yarlagadda, M.K. Carpenter, T.E. Moylan, R.S. Kukreja, R. Koestner, W. Gu, L. Thompson, A. Kongkanand, Boosting Fuel Cell Performance with Accessible Carbon Mesopores, ACS Energy Lett. 3 (2018) 618–621. https://doi.org/10.1021/acsenergylett.8b00186.

[12] G.S. Harzer, J.N. Schwämmlein, A.M. Damjanović, S. Ghosh, H.A. Gasteiger, Cathode Loading Impact on Voltage Cycling Induced PEMFC Degradation: A Voltage Loss Analysis, J. Electrochem. Soc. 165 (2018) F3118–F3131. https://doi.org/10.1149/2.0161806jes.

[13] A. Kongkanand, M.F. Mathias, The Priority and Challenge of High-Power Performance of Low-Platinum Proton-Exchange Membrane Fuel Cells, J. Phys. Chem. Lett. 7 (2016) 1127–1137. https://doi.org/10.1021/acs.jpclett.6b00216.

[14] Y. Garsany, R.W. Atkinson, B.D. Gould, K.E. Swider-Lyons, High power, Low-Pt membrane electrode assemblies for proton exchange membrane fuel cells, J. Power Sources. 408 (2018) 38–

45. https://doi.org/10.1016/j.jpowsour.2018.10.073.

[15] Y. Li, T. Van Cleve, R. Sun, R. Gawas, G. Wang, M. Tang, Y.A. Elabd, J. Snyder, K.C. Neyerlin, Modifying the Electrocatalyst–Ionomer Interface via Sulfonated Poly(ionic liquid) Block Copolymers to Enable High-Performance Polymer Electrolyte Fuel Cells, ACS Energy Lett. (2020) 1726–1731. https://doi.org/10.1021/acsenergylett.0c00532.

[16] K. Kodama, K. Motobayashi, A. Shinohara, N. Hasegawa, K. Kudo, R. Jinnouchi, M. Osawa, Y. Morimoto, Effect of the Side-Chain Structure of Perfluoro-Sulfonic Acid Ionomers on the Oxygen Reduction Reaction on the Surface of Pt, ACS Catal. 8 (2018) 694–700. https://doi.org/10.1021/acscatal.7b03571.

[17] M. Breitwieser, M. Klingele, S. Vierrath, R. Zengerle, S. Thiele, Tailoring the Membrane-Electrode Interface in PEM Fuel Cells: A Review and Perspective on Novel Engineering Approaches, Adv. Energy Mater. 8 (2018). https://doi.org/10.1002/aenm.201701257.

[18] M. Brodt, R. Wycisk, P.N. Pintauro, Nanofiber Electrodes with Low Platinum Loading for High Power Hydrogen/Air PEM Fuel Cells, J. Electrochem. Soc. 160 (2013) 744–749. https://doi.org/10.1149/2.008308jes.

[19] E. Gülzow, T. Kaz, New results of PEFC electrodes produced by the DLR dry preparation technique, J. Power Sources. 106 (2002) 122–125. https://doi.org/10.1016/S0378-7753(01)01030-8.

[20] M. Wang, J.H. Park, S. Kabir, K.C. Neyerlin, N.N. Kariuki, H. Lv, V.R. Stamenkovic, D.J. Myers, M. Ulsh, S.A. Mauger, Impact of Catalyst Ink Dispersing Methodology on Fuel Cell Performance Using in-Situ X-ray Scattering, ACS Appl. Energy Mater. (2019) acsaem.9b01037. https://doi.org/10.1021/acsaem.9b01037.

[21] S. Takahashi, T. Mashio, N. Horibe, K. Akizuki, A. Ohma, Analysis of the Microstructure Formation Process and Its Influence on the Performance of Polymer Electrolyte Fuel-Cell Catalyst Layers, ChemElectroChem. 2 (2015) 1560–1567. https://doi.org/10.1002/celc.201500131.

[22] Y.-C. Park, H. Tokiwa, K. Kakinuma, M. Watanabe, M. Uchida, Effects of carbon supports on Pt distribution, ionomer coverage and cathode performance for polymer electrolyte fuel cells, J. Power Sources. 315 (2016) 179–191. https://doi.org/10.1016/J.JPOWSOUR.2016.02.091.

[23] S.-J. Shin, J.-K. Lee, H.-Y. Ha, S.-A. Hong, H.-S. Chun, I.-H. Oh, Effect of the catalytic ink preparation method on the performance of polymer electrolyte membrane fuel cells, J. Power Sources. 106 (2002) 146–152. https://doi.org/10.1016/S0378-7753(01)01045-X.

[24] T.R. Garrick, T.E. Moylan, V. Yarlagadda, A. Kongkanand, Characterizing Electrolyte and Platinum Interface in PEM Fuel Cells Using CO Displacement, J. Electrochem. Soc. 164 (2017) 5. https://doi.org/10.1149/2.0551702jes.

[25] Y. Liu, M.W. Murphy, D.R. Baker, W. Gu, C. Ji, J. Jorne, H.A. Gasteiger, Proton Conduction and Oxygen Reduction Kinetics in PEM Fuel Cell Cathodes: Effects of Ionomer-to-Carbon Ratio and Relative Humidity, J. Electrochem. Soc. 156 (2009) B970. https://doi.org/10.1149/1.3143965.

[26] T. Van Cleve, S. Khandavalli, A. Chowdhury, S. Medina, S. Pylypenko, M. Wang, K.L. More, N. Kariuki, D.J. Myers, A.Z. Weber, S.A. Mauger, M. Ulsh, K.C. Neyerlin, Dictating Pt-Based Electrocatalyst Performance in Polymer Electrolyte Fuel Cells, from Formulation to Application, ACS Appl. Mater. Interfaces. 11 (2019) 46953–46964. https://doi.org/10.1021/acsami.9b17614.

[27] M.B. Sassin, Y. Garsany, B.D. Gould, K.E. Swider-Lyons, Fabrication Method for Laboratory-Scale High-Performance Membrane Electrode Assemblies for Fuel Cells, Anal. Chem. 89 (2017) 511–518. https://doi.org/10.1021/acs.analchem.6b03005.

[28] M.B. Sassin, Y. Garsany, B.D. Gould, K. Swider-Lyons, Impact of Compressive Stress on MEA Pore Structure and Its Consequence on PEMFC Performance, J. Electrochem. Soc. 163 (2016) F808–F815. https://doi.org/10.1149/2.0291608jes.

[29] Q. Diankai, L. Peng, D. Qiu, H. Janßen, L. Peng, X. Lai, W. Lehnert, Electrical resistance and microstructure of typical gas diffusion layers for proton exchange membrane fuel cell under compression , Appl. Energy. 231 (2018) 127–137. https://doi.org/10.1016/j.apenergy.2018.09.117.

[30] C. Simon, F. Hasché, H.A. Gasteiger, Influence of the Gas Diffusion Layer Compression on the Oxygen Transport in PEM Fuel Cells at High Water Saturation Levels, J. Electrochem. Soc. 164 (2017) F591–F599. https://doi.org/10.1149/2.0691706jes.

[31] J. Ge, A. Higier, H. Liu, Effect of gas diffusion layer compression on PEM fuel cell performance, J. Power Sources. 159 (2006) 922–927. https://doi.org/10.1016/j.jpowsour.2005.11.069.

[32] H. Lv, D. Li, D. Strmcnik, A.P. Paulikas, N.M. Markovic, V.R. Stamenkovic, Recent advances in the design of tailored nanomaterials for efficient oxygen reduction reaction, 2016. https://www.sciencedirect.com/science/article/pii/S2211285516300556 (accessed September 25, 2019).

[33] X.X. Wang, J. Sokolowski, H. Liu, G. Wu, Pt alloy oxygen-reduction electrocatalysts: Synthesis, structure, and property, Chinese J. Catal. 41 (2020) 739–755. https://doi.org/10.1016/S1872-2067(19)63407-8.

[34] S. Sharma, B.G. Pollet, Support materials for PEMFC and DMFC electrocatalysts - A review, J. Power Sources. 208 (2012) 96–119. https://doi.org/10.1016/j.jpowsour.2012.02.011.

[35] M. Uchida, PEFC catalyst layers: Effect of support microstructure on both distributions of Pt and ionomer and cell performance and durability, Curr. Opin. Electrochem. 21 (2020) 209–218. https://doi.org/10.1016/j.coelec.2020.02.019.

[36] X. Yu, S. Ye, Recent advances in activity and durability enhancement of Pt/C catalytic cathode in PEMFC. Part I. Physico-chemical and electronic interaction between Pt and carbon support, and activity enhancement of Pt/C catalyst, J. Power Sources. 172 (2007) 133–144. https://doi.org/10.1016/j.jpowsour.2007.07.049.

[37] S. Shahgaldi, I. Alaefour, X. Li, The impact of short side chain ionomer on polymer electrolyte membrane fuel cell performance and durability, Appl. Energy. 217 (2018) 295–302. https://doi.org/10.1016/j.apenergy.2018.02.154.

[38] K. Talukdar, P. Gazdzicki, K.A. Friedrich, Comparative investigation into the performance and durability of long and short side chain ionomers in Polymer Electrolyte Membrane Fuel Cells, J. Power Sources. 439 (2019) 227078. https://doi.org/10.1016/j.jpowsour.2019.227078.

[39] S. Khandavalli, J.H. Park, N.N. Kariuki, D.J. Myers, J.J. Stickel, K. Hurst, K.C. Neyerlin, M. Ulsh, S.A. Mauger, Rheological Investigation on the Microstructure of Fuel Cell Catalyst Inks, ACS Appl. Mater. Interfaces. (2018). https://doi.org/10.1021/acsami.8b15039.

[40] A. Orfanidi, P.J. Rheinländer, N. Schulte, H.A. Gasteiger, Ink Solvent Dependence of the Ionomer Distribution in the Catalyst Layer of a PEMFC, J. Electrochem. Soc. (2018). https://doi.org/10.1149/2.1251814jes.

[41] G. Wang, L. Osmieri, A.G. Star, J. Pfeilsticker, K.C. Neyerlin, Elucidating the Role of Ionomer in the Performance of Platinum Group Metal-free Catalyst Layer via in situ Electrochemical Diagnostics, J. Electrochem. Soc. 167 (2020) 044519. https://doi.org/10.1149/1945-7111.

[42] L. Osmieri, G. Wang, F.C. Cetinbas, S. Khandavalli, J. Park, S. Medina, S.A. Mauger, M. Ulsh, S. Pylypenko, D.J. Myers, K.C. Neyerlin, Utilizing ink composition to tune bulk-electrode gas transport, performance, and operational robustness for a Fe–N–C catalyst in polymer electrolyte fuel cell, Nano Energy. (2020) 104943. https://doi.org/10.1016/j.nanoen.2020.104943.

[43] S. Kabir, D.J. Myers, N.N. Kariuki, J. Park, G. Wang, A. Baker, N. Macauley, R. Mukundan, K.L. More, K.C. Neyerlin, Elucidating the Dynamic Nature of Fuel Cell Electrodes as a Function of Conditioning: An Ex-situ Materials Characterization and In-situ Electrochemical Diagnostic Study, (2019). https://doi.org/10.1021/acsami.9b11365.

[44] R. Makharia, M.F. Mathias, D.R. Baker, Measurement of Catalyst Layer Electrolyte Resistance in PEFCs Using Electrochemical Impedance Spectroscopy, J. Electrochem. Soc. 152 (2005) A970. https://doi.org/10.1149/1.1888367.

[45] D.R. Baker, D.A. Caulk, K.C. Neyerlin, M.W. Murphy, Measurement of Oxygen Transport Resistance in PEM Fuel Cells by Limiting Current Methods, J. Electrochem. Soc. 156 (2009) 13. https://doi.org/10.1149/1.3152226.

[46] Hydrogen Storage Technologies Roadmap Fuel Cell Technical Team Roadmap, 2013. www.uscar.org. (accessed May 31, 2020).

[47] J. Ilavsky, P.R. Jemian, A.J. Allen, F. Zhang, L.E. Levine, G.G. Long, IUCr, Ultra-small-angle X-ray scattering at the Advanced Photon Source, J. Appl. Crystallogr. 42 (2009) 469–479. https://doi.org/10.1107/S0021889809008802.

[48] J. Ilavsky, *Nika* : software for two-dimensional data reduction, J. Appl. Crystallogr. 45 (2012) 324–328. https://doi.org/10.1107/S0021889812004037.

[49] J. Ilavsky, P.R. Jemian, *Irena* : tool suite for modeling and analysis of small-angle scattering, J. Appl. Crystallogr. 42 (2009) 347–353. https://doi.org/10.1107/S0021889809002222.

[50] P.R. Jemian, J.R. Weertman, G.G. Long, R.D. Spal, Characterization of 9Cr-1MoVNb steel by anomalous small-angle X-ray scattering, Acta Metall. Mater. 39 (1991) 2477–2487. https://doi.org/10.1016/0956-7151(91)90062-6.

[51] R. Borup, FC-PAD: Fuel Cell Performance and Durability Consortium, Annual Merit Review 2018, (2018) 67. https://www.hydrogen.energy.gov/pdfs/review18/fc135_borup_2018_o.pdf.

[52] F.C. Cetinbas, R.K. Ahluwalia, N.N. Kariuki, V. De Andrade, D.J. Myers, Effects of Porous Carbon Morphology, Agglomerate Structure and Relative Humidity on Local Oxygen Transport Resistance, J. Electrochem. Soc. 167 (2020) 013508. https://doi.org/10.1149/2.0082001jes.

[53] D.M. Pelt, D. Gürsoy, W.J. Palenstijn, J. Sijbers, F. De Carlo, K.J. Batenburg, Integration of TomoPy and the ASTRA toolbox for advanced processing and reconstruction of tomographic synchrotron data, J. Synchrotron Radiat. 23 (2016) 842–849. https://doi.org/10.1107/S1600577516005658.

[54] V. De Andrade, A. Deriy, M.J. Wojcik, D.G.¨ Ursoy, D. Shu, K. Fezzaa, F. De Carlo, Nanoscale 3D imaging at the Advanced Photon Source, (n.d.). https://doi.org/10.1117/2.1201604.006461.

[55] F.C. Cetinbas, R.K. Ahluwalia, N.N. Kariuki, D.J. Myers, Agglomerates in Polymer Electrolyte Fuel Cell Electrodes: Part I. Structural Characterization, J. Electrochem. Soc. 165 (2018) F1051–F1058. https://doi.org/10.1149/2.0571813jes.

[56] F.C. Cetinbas, R.K. Ahluwalia, Agglomerates in Polymer Electrolyte Fuel Cell Electrodes: Part II. Transport Characterization, J. Electrochem. Soc. 165 (2018) F1059–F1066. https://doi.org/10.1149/2.0301813jes.

[57] F.C. Cetinbas, X. Wang, R.K. Ahluwalia, N.N. Kariuki, R.P. Winarski, Z. Yang, J. Sharman, D.J. Myers, Microstructural Analysis and Transport Resistances of Low-Platinum-Loaded PEFC Electrodes, J. Electrochem. Soc. 164 (2017) F1596–F1607. https://doi.org/10.1149/2.1111714jes.

[58] S. Komini Babu, H.T. Chung, P. Zelenay, S. Litster, Resolving Electrode Morphology's Impact on Platinum Group Metal-Free Cathode Performance Using Nano-CT of 3D Hierarchical Pore and Ionomer Distribution, ACS Appl. Mater. Interfaces. 8 (2016) 32764–32777. https://doi.org/10.1021/acsami.6b08844.

[59] T. Schuler, A. Chowdhury, A.T. Freiberg, B. Sneed, F.B. Spingler, M.C. Tucker, K.L. More, C.J. Radke, A.Z. Weber, Fuel-Cell Catalyst-Layer Resistance via Hydrogen Limiting-Current Measurements, J. Electrochem. Soc. 166 (2019) F3020–F3031. https://doi.org/10.1149/2.0031907jes.

[60] D. Novitski, S. Holdcroft, Determination of O2 Mass Transport at the Pt | PFSA Ionomer Interface under Reduced Relative Humidity, ACS Appl. Mater. Interfaces. 7 (2015) 27314–27323. https://doi.org/10.1021/acsami.5b08720.

[61] K. Kudo, R. Jinnouchi, Y. Morimoto, Humidity and Temperature Dependences of Oxygen Transport Resistance of Nafion Thin Film on Platinum Electrode, Electrochim. Acta. 209 (2016) 682–690. https://linkinghub.elsevier.com/retrieve/pii/S0013468616308118 (accessed April 3, 2019).

[62] J.P.J.E. Owejan, J.P.J.E. Owejan, W. Gu, Impact of Platinum Loading and Catalyst Layer Structure on PEMFC Performance, J. Electrochem. Soc. 160 (2013) F824–F833. https://doi.org/10.1149/2.072308jes.

[63] T.A. Greszler, D. Caulk, P. Sinha, The Impact of Platinum Loading on Oxygen Transport Resistance, J. Electrochem. Soc. 159 (2012) F831–F840. https://doi.org/10.1149/2.061212jes.

[64] R. Darling, Modeling Air Electrodes with Low Platinum Loading, J. Electrochem. Soc. 166 (2019) F3058–F3064. https://doi.org/10.1149/2.0101907jes.

[65] H. Iden, A. Ohma, An in situ technique for analyzing ionomer coverage in catalyst layers, J. Electroanal. Chem. 693 (2013) 34–41. https://doi.org/10.1016/j.jelechem.2013.01.026.

[66] J. Clavilier, R. Albalat, R. Gomez, J.M. Orts, J.M. Feliu, A. Aldaz, Study of the charge displacement at constant potential during CO adsorption on Pt(110) and Pt(111) electrodes in contact with a perchloric acid solution, J. Electroanal. Chem. 330 (1992) 489–497. https://doi.org/10.1016/0022-0728(92)80326-Y.

[67] S.A. Berlinger, B.D. McCloskey, A.Z. Weber, Inherent Acidity of Perfluorosulfonic Acid Ionomer

Dispersions and Implications for Ink Aggregation, J. Phys. Chem. B. 122 (2018) 7. https://doi.org/10.1021/acs.jpcb.8b06493.

[68] K.B. Hatzell, M.B. Dixit, S.A. Berlinger, A.Z. Weber, Understanding inks for porous-electrode formation, J. Mater. Chem. A. 5 (2017) 20527–20533. https://doi.org/10.1039/C7TA07255D.

[69] M.A. Modestino, A. Kusoglu, A. Hexemer, A.Z. Weber, R.A. Segalman, Controlling Nafion Structure and Properties via Wetting Interactions, Macromolecules. 45 (2012) 4681–4688. https://doi.org/10.1021/ma300212f.

[70] A. Kusoglu, D. Kushner, D.K. Paul, K. Karan, M.A. Hickner, A.Z. Weber, Impact of Substrate and Processing on Confinement of Nafion Thin Films, Adv. Funct. Mater. 24 (2014) 4763–4774. https://doi.org/10.1002/adfm.201304311.

[71] K. Kinoshita, Carbon—Electrochemical and Physicochemical Properties., Wiley, New York, 1988. https://doi.org/10.1002/ange.19881000944.

[72] M. Eikerling, Water Management in Cathode Catalyst Layers of PEM Fuel Cells, J. Electrochem. Soc. 153 (2006) E58. https://doi.org/10.1149/1.2160435.

[73] T. Soboleva, X. Zhao, K. Malek, Z. Xie, T. Navessin, S. Holdcroft, On the micro-, meso-, and macroporous structures of polymer electrolyte membrane fuel cell catalyst layers, ACS Appl. Mater. Interfaces. 2 (2010) 375–384. https://doi.org/10.1021/am900600y.

[74] G. Nichols, S. Byard, M.J. Bloxham, J. Botterill, N.J. Dawson, A. Dennis, V. Diart, N.C. North, J.D. Sherwood, A review of the terms agglomerate and aggregate with a recommendation for nomenclature used in powder and particle characterization, J. Pharm. Sci. 91 (2002) 2103–2109. https://doi.org/10.1002/jps.10191.

[75] J.S. Spendelow, Advanced Electro-Catalysts through Crystallographic Enhancement, 2020 DOE Fuel Cell Technol. Off. Annu. Merit Rev. (2020) 35. https://www.hydrogen.energy.gov/pdfs/review19/fc161_spendelow_2019_o.pdf (accessed July 30, 2020).

[76] A. Kongkanand, Highly-Accessible Catalysts for Durable High-Power Performance, 2019 AMR FC144, DOE FCTO Annu. Reports. (2018) 1–31. https://www.hydrogen.energy.gov/pdfs/review19/fc144_kongkanand_2019_o.pdf (accessed July 30, 2020).

[77] S. Kumaraguru, Durable High-Power Membrane Electrode Assembly with Low Platinum Loading, 2020. https://www.hydrogen.energy.gov/pdfs/review14 (accessed August 3, 2020).

Graphical TOC (5x13 cm)